*Acta Polytechnica* **65**(3):263–275, 2025
https://doi.org/10.14311/AP.2025.65.0263

Published by the Czech Technical University in Prague

# DETERMINATION OF MECHANICAL PROPERTIES OF VERY THIN 3D-PRINTED SPECIMENS FOR NUMERICAL ANALYSIS OF TENSILE STRENGTH AND FRACTURE TOUGHNESS

Petr Bočan*, Aleš Jíra

*Czech Technical University in Prague, Faculty of Civil Engineering, Department of Mechanics, Thákurova 7, 166 29 Prague, Czech Republic*

* corresponding author: petr.bocan@fsv.cvut.cz

Abstract. This research deals with the influence of thickness on the mechanical properties of polyamide (PA12) samples produced by the SLS 3D technology. Experiments included fracture toughness and simple tensile tests on samples with thicknesses ranging from 0.50 mm to 2.00 mm. The experiment revealed that the thickness of the specimen significantly affected the tensile strength and Young's modulus. The measured tensile strength (22–34 MPa) was notably lower than the 41 MPa reported by the manufacturer. As a result, a numerical analysis using ATENA software showed substantial discrepancies between the FEA predictions and the experimental data. This led to a modification of the material model and the determination of the effective Young's modulus fit to thin polyamide samples, which improved the agreement of the numerical and experimental data.

Keywords: Fracture mechanics, simple tensile, numerical analysis, 3D printing, polyamide PA12.

## 1. Introduction

3D printing technology is currently one of the most progressive additive manufacturing methods in many industries. This technology allows for the model of more complex structures and opens the door to many innovations, which is why this type of manufacturing is currently being widely explored.

In the biomedical industry, 3D printing is important in the development of intraosseous implants. This technology offers the possibility of creating porous structures on the surface of implants that connect bone and implant by bone cells that grow in the pores and provide interaction between bone and implant [1, 2]. Trabecular and gyroid structures are the two main types commonly used on the surface of implants [3]. These porous structures are composed of beams (trabecular) or walls (gyroid) systems that provide mechanical loading capacity.

In the production of trabecular structures for the implant surface, the thickness of the beams is around 150–350 µm. The research of the TAČR project [4] shows large discontinuities between beams and weakening of the beam cross-section (Figure 1). Therefore, the concept of trabecular structures has been replaced by a more reliable gyroid structure that is less prone to local defects [3]. The gyroid is a continuous structure with a periodic morphology, constant curvature, and interconnected open pores [5]. However, the gyroid structure uses very thin structural elements (walls) with a thickness of about 150–350 µm, which is the printing limit for 3D printing technology nowadays.

Unfortunately, the gyroid structure also exhibits significant defects, which subsequently cause differences between the experimental results and the numerical analysis. These defects are caused by imperfect welding of powder balls, which fall off and thus weaken the thickness of the supporting structure. Bending and simple tension experiments [7] showed that the mechanical properties guaranteed by the manufacturer cannot be taken into account for 3D printed specimens of thin thickness. It is necessary to determine the degree of inaccuracy and deviation of the actual properties from the experiment and theoretical ones, to replace expensive and complex experiments with numerical solutions.

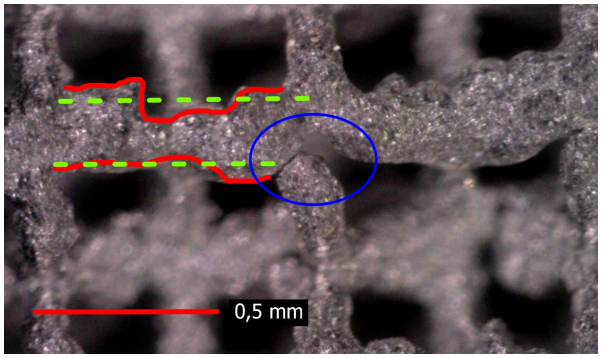


Figure 1. Example of trabecular structure defects produced using 3D printing technology [4].

All of the studies mentioned above dealt with the mechanical properties of the titanium alloy $Ti_6Al_4V$, which is currently the most widely used alloy for the production of intraosseous implants. However, this material is expensive to produce, so the research was conducted on polyamide PA12, where printing polyamides is much cheaper and more accessible.

Nowadays, the nylon materials can be taken into account as a potential replacement for metal implants [8],

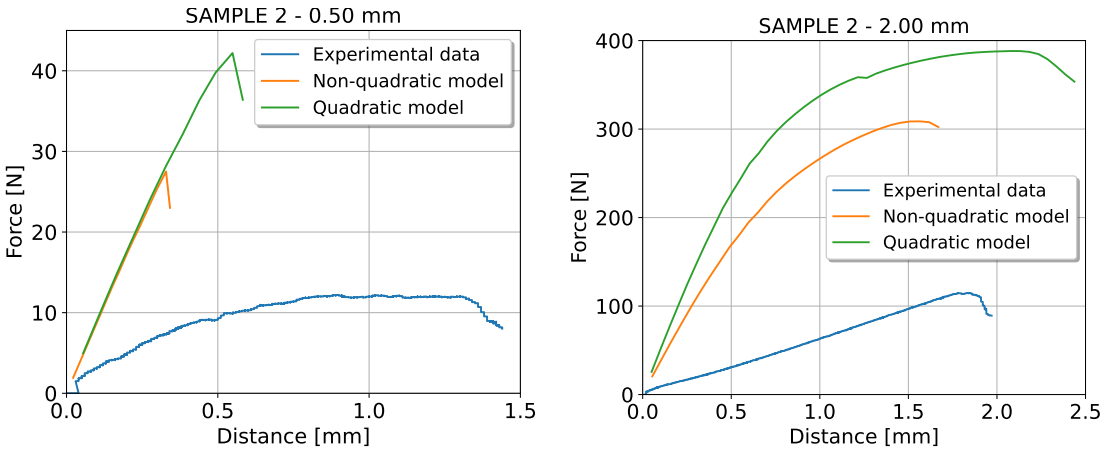


Figure 2. Comparison of experimental data with numerical analysis for the fracture toughness case [6].

due to their bio compatibility, chemical stability, tunable mechanical qualities, and ability to be manufactured by 3D printing technology [9]. Nylon is used mainly in the dental industry, where the advantage of using this material is that it is not that expensive to produce. However, the service life of a nylon implant is shorter than that of the metal one [10]. The second usage for nylon materials in bioapplication is an external fixation sleeves, which can be designed and used for the patient's needs [11]. All this mentioned use of nylon material in the medical industry leads to the same problem as in the use of metal materials, where the load-bearing elements of the structure are very thin and it is necessary to study nylon material for this application.

It is crucial to understand the defects during the 3D printing manufacturing of nylon materials. One of the defects is the porosity of the printed samples. Since nylon materials undergo thermal processes with temperature profiles that introduce meso- or micro-heterogeneities such as voids and pores into the printed parts [12]. These types of defect could influence the mechanical properties of the final parts [13]. Another problem accompanying powder printing is the shrinkage and warping of the material. Shrinkage is caused by the cyclic heating and cooling of each layer during the manufacturing process and is divided into two forms: sintering shrinkage and thermal shrinkage. Warping is also a defect caused by shrinkage due to an increase in internal stresses during printing process. It is caused by the recoating process, in which a heated layer is applied with a lower temperature. This causes a heat exchange in the different regions, leading to non-uniform temperature gradients that result in an internal stress build-up. [12].

Rodríguez et al. [14] evaluated the mechanical properties in a tensile experiment with different thicknesses and proved that thickness slightly influences the tensile strength. In addition, the SEM images of the sample surface in this study showed insufficient sintering of the powder balls on the sample porosity, which leads to a change in the cross-section of the sample and can significantly affect its mechanical properties. Other studies [15, 16] showed that for thinner samples (up to 0.6 mm thick) with standard shape, the tensile strength of the sample is significantly reduced. Studies on components or whole structures have subsequently also shown this trend [17, 18].

Previous research [6] was about the fracture toughness of very thin polyamide samples produced by SLS 3D printing technology. The experiment was designed according to a suitable standard from which the geometry of the samples, the experimental procedure, and the final fracture toughness calculation were used. The experiment was carried out on samples with widths ranging from 0.50 to 2.00 mm. The ortotrophy of 3D printing was accounted for by varying the orientation of the print, where layers were printed perpendicular or parallel to the expected crack propagation. A more detailed description of the experiment and results is given in Section 3.1.

The research complemented the numerical analysis calculated in the ATENA software [20]. The geometry of the numerical model copied the experimental sample geometry, and a basic material model was determined. The datasheet for PA12 [21] contains only basic mechanical parameters such as Young's modulus, tensile strength, and elongation at break. Therefore, mechanical parameters, such as compressive strength and fracture energy, had to be retrieved from other experiments for the numerical analysis. Unfortunately, the comparison of the experimental data and the numerical analysis data showed significant differences as seen in Figure 2.

These large differences led us to take a closer look at the numerical analysis and detect errors that may be causing the differences. The diagrams show that the linear part of the experimental data and the numerical analysis do not match, which seems to be the first problem. This is probably due to the chosen material model, where for thin samples, the guaranteed mechanical properties cannot be taken from a datasheet.

Based on this, a simple tensile experiment was designed for a thin PA12 sample. It should show the

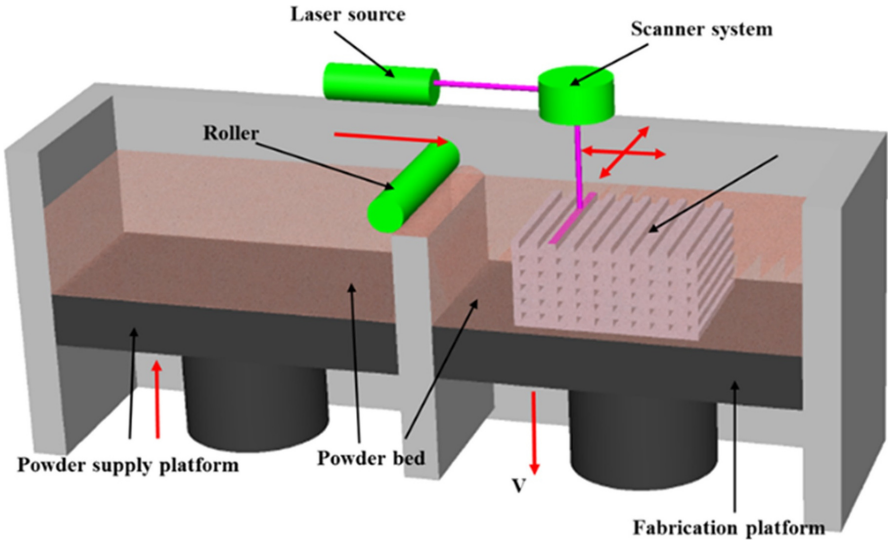


FIGURE 3. Schematic representation of SLS technology printing process [19].

actual behaviour of the thin samples in their linear part. Then, the effective Young's modulus and ultimate tensile strength for these samples can be easily determined in the numerical model for this type of loading (simple tensile) in numerical analysis. Once the mechanical parameters for the simple tensile numerical analysis are determined and agree with the experimental data, they can then be used for the numerical analysis of fracture toughness.

## 2. Material and method of manufacture

The experiment examined PA12 Smooth by Sinterit sp. z o.o. processed by SLS 3D printing technology. Nylons are an important part of the thermoplastic polymer family and are also known as polyamides (PA) due to their repeating units connected by amide bonds. There are many subtypes with different crystal structures and material properties (Nylon 6, Nylon 12, Nylon 66, and others) [22]. Nylon 12 has longer aliphatic chains than other polyamides, which causes high pressure resistance, flexibility of impact resistance, low density, and good mechanical resistance [23].

Powder bed fusion (PBF), also known as selective laser sintering (SLS), is one of many printing methods for additive manufacture. It is often used for printing metal and polyamide parts. This technology fuses powder balls in layers with a high heat source. Pulsed laser, electron beam, or ultraviolet light can be used as heat sources [24]. Figure 3 shows a schematic representation of the SLS 3D printing process.

Nowadays, 3D printing technologies are commonly used for additive manufacturing in many industries. The problem of SLS technology in powder printing starts with thin samples, where one of the significant weaknesses is the inadequately welded powder balls and the other is the inconsistent sample width. Inadequately welded powder balls subsequently fall off

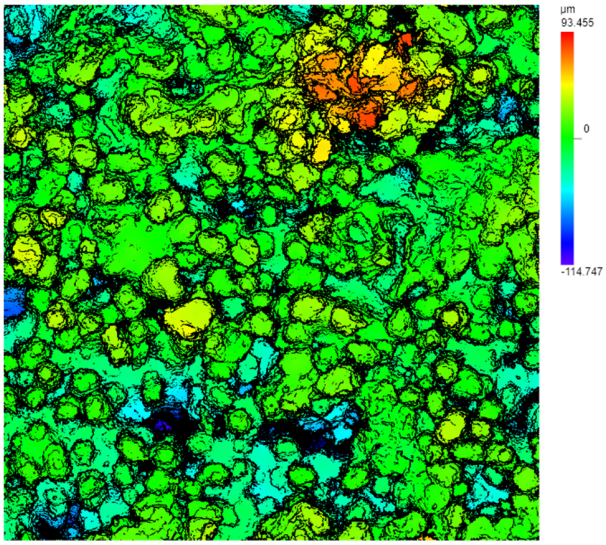


FIGURE 4. The result of the confocal microscope measurement, showing in the detail unevenness of the sample surface [6].

during sample handling, and this causes a weakening of the sample width, leading to a reduction in load-carrying capacity and basic mechanical properties such as modulus of elasticity. Figure 4 shows the roughness and differences in thicknesses on the sample surface measured with a confocal microscope. These differences can easily reduce the width of the specimens and affect the values in the experiments and subsequent calculation of mechanical properties.

## 3. Experimental part

Two types of experiments were conducted to validate the results of the numerical analysis. Initially, an experiment on fracture toughness [6], followed by a complementary simple tensile test was carried out. Both experiments involved specimens with widths ranging from 0.50 mm to 2.00 mm, with geometries according

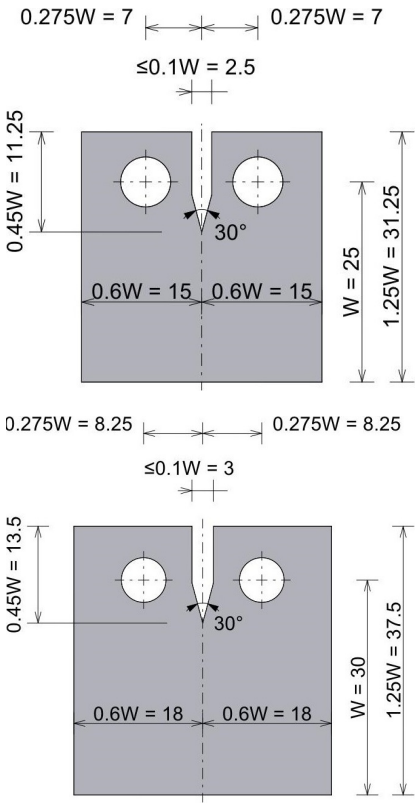


Figure 5. The geometries of specimens for fracture toughness experiment according to EN ISO 12737 [25]. The upper picture is SAMPLE 2, and the lower picture is SAMPLE 3 [6].

to relevant standards. A Mark 10 load press was used to apply the loads in both experiments. The fracture toughness test was further improved with 3D macro Digital Image Correlation (DIC) to monitor crack propagation and measure crack length, providing real-time, high-precision data throughout the experiment.

### 3.1. Fracture toughness experiment

The fracture toughness experiment was carried out according to EN ISO 1273 [25]. With minor modifications, the geometry of the specimens, the experiment procedure, and the final calculation of the fracture toughness value were taken from the standard. In the last research [6], I investigated the fracture toughness of two specimen geometries as shown in Figure 5.

These geometries were selected after a pre-test experiment on four different geometries. The dimensions of these specimens showed the most linear increase in values due to the sample thickness and the best handling during the experiment. Finally, compared to SAMPLE 4, which had the largest dimensions, there was not as much torsion at the free end during the loading, which subsequently affected the results.

The orthotropy of the material was considered by using different printing directions, referred to as H (horizontal) and V (vertical). Orthotropy refers to the characteristic of a material having varying properties along different perpendicular axes, which is typical for

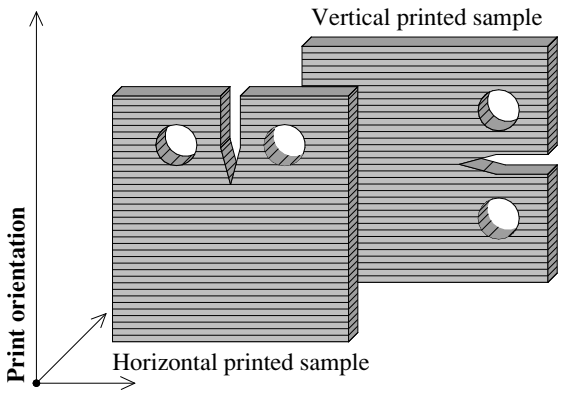


Figure 6. Schematic of the proposed printing direction to account for the orthotropy of the material [6].

composite materials. Figure 6 illustrates the schematic of the proposed printing directions, showing how the material's mechanical behaviour changes depending on the orientation of the print layers.

According to standard EN ISO 1273 [25], the calculation of fracture toughness values, follows the exact solution for the critical stress intensity factor $K_Q$ as shown in:

$$K_Q = \frac{F_Q}{B\sqrt{W}} * f_{(a/W)}, \tag{1}$$

where $F_Q$ is the force determined from the experiment data, $B$ is the sample thickness, and $W$ is the length of the ligament. An essential parameter in the calculation is the geometric factor $f_{(a/W)}$, which is a dimensionless function of $\frac{a}{W}$. The final result of the fracture toughness $K_Q$ is shown in Table 1 and Figure 7.

### 3.2. Tensile experiment

According to EN ISO 527-1, 2 [26, 27], a tensile experiment was performed. The main object of the experiment was to determine the ultimate tensile strength of very thin specimens. The second objective was to take a closer look at the linear behaviour of thin samples in a simple tensile experiment. The geometry of the specimens given by the standard is shown in Figure 8.

The ortotrophy of the material was accounted for by using a different print orientation, as was the case for fracture toughness. Vertically printed specimens had layers printed parallel to the tension load, while horizontally printed specimens had layers perpendicular to the tensile load. Figure 9 shows a schematic example of printing samples for botch print orientations.

The experiment showed a problem with loading thin specimens, especially specimens with a width of 0.50 mm. Inserting these specimens into the grips damaged the expanded part of the specimens, causing deformation in this part, as can be seen in Figure 10.

For this reason, these specimens were marked as defective measuring pieces and are not included in the final tensile strength evaluation. Figure 11 shows the L-D diagram values for the 0.50 mm thick specimens.

| Thickness [mm] | 0.50 | 0.75 | 1.00 | 1.25 | 1.50 | 2.00 |
|---|---|---|---|---|---|---|
| SAMPLE 2 – H | $2.00 \pm 0.60$ | $2.64 \pm 1.12$ | $1.65 \pm 0.23$ | $1.87 \pm 0.09$ | $2.16 \pm 0.45$ | $2.37 \pm 0.31$ |
| SAMPLE 2 – V | $0.99 \pm 0.37$ | $0.91 \pm 0.38$ | $0.93 \pm 0.11$ | $1.35 \pm 0.35$ | $0.94 \pm 0.07$ | $1.09 \pm 0.15$ |
| SAMPLE 3 – H | $1.54 \pm 0.22$ | $1.33 \pm 0.48$ | $1.50 \pm 0.15$ | $1.73 \pm 0.38$ | $2.01 \pm 0.33$ | $2.20 \pm 0.36$ |
| SAMPLE 3 – V | $1.20 \pm 0.41$ | $0.72 \pm 0.11$ | $1.30 \pm 0.42$ | $1.03 \pm 0.06$ | $1.21 \pm 0.15$ | $1.09 \pm 0.15$ |

TABLE 1. Summary of fracture toughness results $K_Q$ obtained in the experiment, where H denotes horizontally printed specimens and V denotes vertically printed specimens [6].

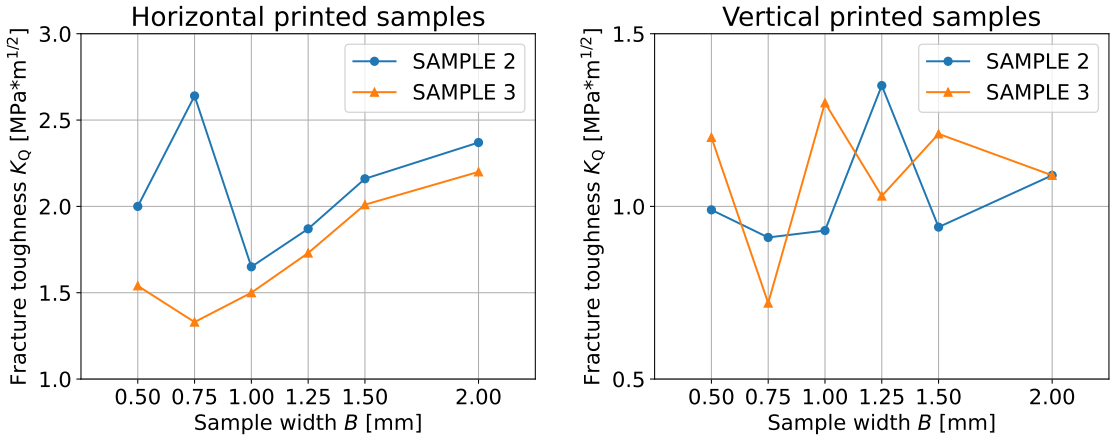


FIGURE 7. Final fracture toughness results for individual sample thicknesses with different printing directions [6].

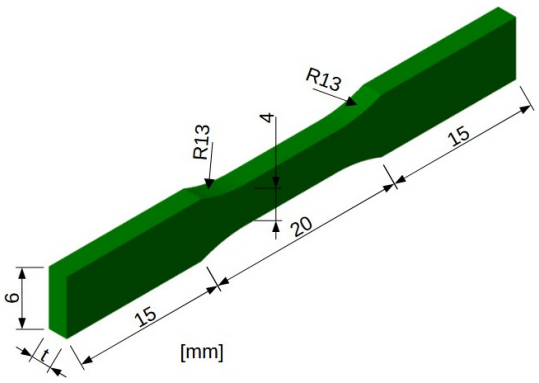


FIGURE 8. Geometry of dog bone used in the experiment with variable widths from 0.50 to 2.00 mm.

FIGURE 10. Example of 0.50 mm thick samples after measurement, where you can see defective samples that cannot be evaluated.

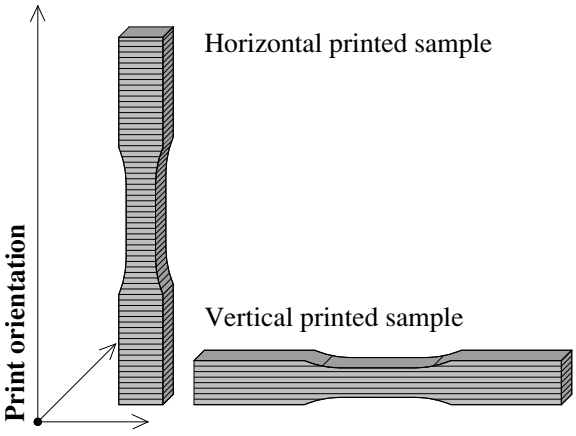


FIGURE 9. Samples print orientation for horizontal and vertical samples.

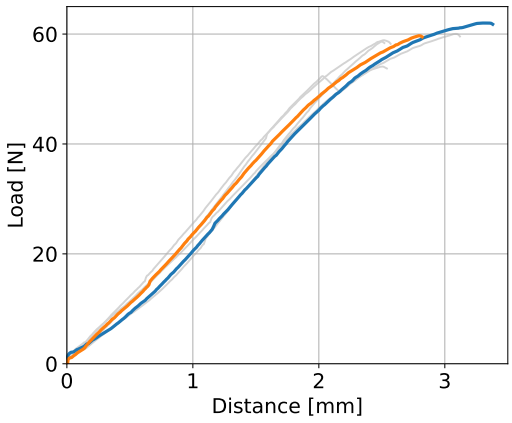


FIGURE 11. Load-distance diagrams show the selected values for the tensile strength calculation – the colored lines are the selected files for the calculation, and the gray shaded lines are the defective samples.

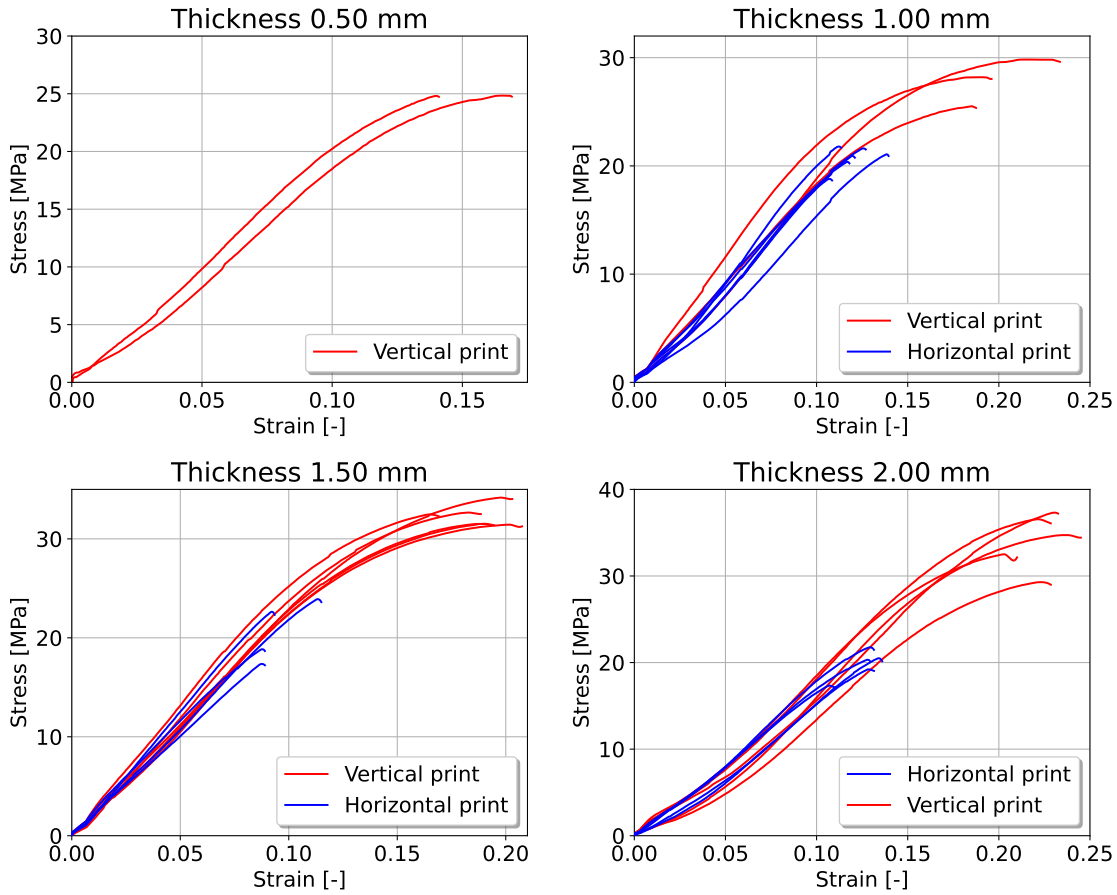


Figure 12. Stress–strain diagrams for specimens with widths 0.50, 1.00, 1.50, and 2.00 mm. Blue curves indicate samples printed in the horizontal direction, and red curves indicate samples printed in the vertical direction.

The color curves are then used in the final evaluation of the tensile strength value.

This resulted in the experiment being conducted on a limited number of samples, making the results for this thickness not sufficiently reliable. The same applies to the 1.25 mm thick samples, for which three samples were only printed. The other samples had a sufficient sample number for their result to be taken as relevant. In the experiment, there were differences in the result for vertically and horizontally printed specimens, especially in the maximum load for specimen breakage. Figure 12 shows these differences for each print orientation.

From these measurement data was calculated the ultimate tensile strength of each specimen width. The ultimate tensile strength for each specimen was calculated as:

$$f_t = \frac{F_{max}}{A_0}, \tag{2}$$

where $f_t$ is the tensile strength, $F_{max}$ is the maximal force from experiment data and $A_0$ is the cross-section area measured for each samples.

Table 2 and Table 3 show the tensile strength results for each specimen width in both print directions. No values are given for the horizontal printed specimens of 0.50 mm and 1.25 mm width due to inadequate handling during the experiment or the small number of specimens for the experiment.

| **Samples widths [mm]** | **Tensile strength [MPa]** |
|---|---|
| 0.50 | $25.30 \pm 0.06$ |
| 0.75 | $22.61 \pm 1.55$ |
| 1.00 | $28.26 \pm 1.87$ |
| 1.25 | $32.51 \pm 1.19$ |
| 1.50 | $32.48 \pm 0.97$ |
| 2.00 | $34.24 \pm 2.88$ |

Table 2. Tensile strength for the vertically print samples.

| **Samples widths [mm]** | **Tensile strength [MPa]** |
|---|---|
| 0.50 | - |
| 0.75 | $11.76 \pm 1.04$ |
| 1.00 | $21.29 \pm 0.95$ |
| 1.25 | - |
| 1.50 | $21.16 \pm 2.62$ |
| 2.00 | $20.07 \pm 1.45$ |

Table 3. Tensile strength for the horizontally print samples.

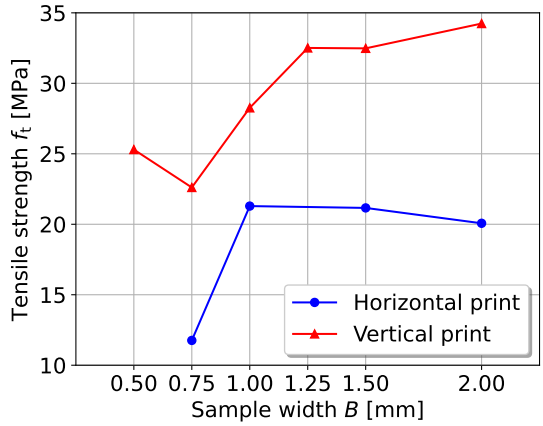


FIGURE 13. Overview of tensile strength values depending on specimen thickness.

As expected, the values for vertically printed samples were greater than those for horizontally printed samples, which is because vertically printed specimens have layers printed parallel to the loading. Thus, more stress is required to break their layers. Whereas horizontally printed specimens have layers perpendicular to the loading, so less stress was needed to break the specimen. In this fact, the horizontally printed specimens often fractured in the middle of the tapered part of the specimen compared to the vertically printed specimens.

Both printed directions show a large value increase between widths 0.75 mm and 1.00 mm. For horizontally printed samples the values then increase slightly, while for vertically printed samples they are around the same value, as shown in Figure 13.

Anyway, the PA12 technical datasheet [21] gives a tensile strength value of 41 MPa, which is still much higher than the highest value taken from the experiment, which proves that for thin specimens the manufacturer's certified values cannot be considered at present.

Due to the small number of samples tested in horizontal printed orientation, the calculation of Young's modulus was solved only for vertically printed samples. Subsequently, the experimental results for this printing orientation are verified by numerical analysis. The formula for calculating Young's modulus solved in the linear part of each test sample can be obtained as follows:

$$E = \frac{\sigma}{\epsilon}, \tag{3}$$

where stress was determined as $\sigma = \frac{F}{A}$ and strain as $\epsilon = \frac{\Delta L}{L_0}$. Unfortunately, the length between grips was not measured during the experiment, so the original length $L_0$ had to be set to 20 mm, which is the length of the narrowed part. For this reason, it had to be emphasized that Young's modulus results here serve only as an indication for subsequent investigation of the value by numerical analysis.

The result shows an increase in values with increasing thickness, as shown in Table 4.

| **Samples widths [mm]** | **Young's Modulus [MPa]** |
|---|---|
| 0.50 | $215.75 \pm 8.38$ |
| 0.75 | $209.66 \pm 17.29$ |
| 1.00 | $212.61 \pm 25.48$ |
| 1.25 | $250.34 \pm 10.50$ |
| 1.50 | $254.24 \pm 13.51$ |
| 2.00 | $260.01 \pm 14.17$ |

TABLE 4. Young's modulus for the vertically print samples.

The results of Young's modulus measurements again showed that the values for very thin samples are much lower than the values given by the manufacturer. In Section 4, the value of Young's modulus is investigated using numerical analysis to approximate the agreement between the experiment and numerical analysis results.

## 4. NUMERICAL ANALYSIS

The numerical model was created using GiD 16.0.6 software, which served as a preprocessor for numerical analysis. The finite element analysis (FEA) was carried out in ATENA 2024 software [20], which served for the nonlinear concrete structure analysis. Still, this software can also be used with appropriately chosen material models for other materials. This software is effective for the numerical simulation of experiments, for the crack progression initiation and determination of the maximum load capacity before failure.

ATENA software allows the calculation to be performed by three different iterative methods to solve nonlinear equations (Full Newton-Raphson method, Modified Newton-Raphson method and Arc-length method). In my case, the experiment simulation used deformation as a displacement controlled, so I used the Full Newton-Raphson method in the calculation. The method looks for a solution in the tangent direction at the initial point of the calculation step, where the tangent stiffness matrix gives the direction in the continuum [28]. The calculation is divided into several steps with several iterations, and in each iteration, a new tangent stiffness matrix is calculated. The loading step ends when the condition of an admissible difference between successive iterations is satisfied [29]. A schematic description of the Newton-Raphson iterative method is shown in Figure 14.

As described in the introduction, the manufacturer provides insufficient information on the mechanical parameters of the PA12 material. The applicable parameters for FEA from the manufacturer's datasheet include density $\rho = 1\,010\,\mathrm{kg\,m^{-3}}$, Young's modulus $E = 1.47$ GPa, ultimate tensile strength $f_{t,u} = 41$ MPa and elongation at break $\epsilon_u = 0.13$ [21]. In this fact, the value of the fracture energy $G_f$ and the Poisson's ration $\mu$ had to be determined from another experiment. Other research has shown that the values

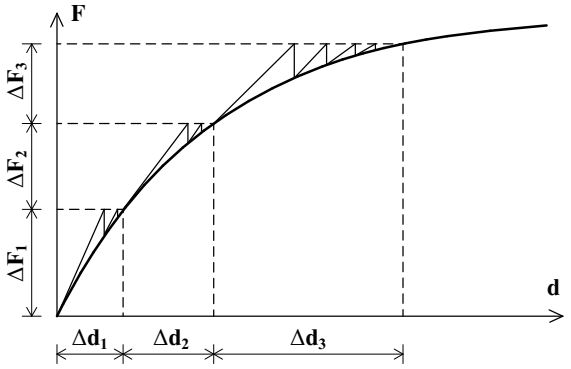


Figure 14. Full Newton-Raphson method for FEA used in structural problems, where $F$ is the load and $d$ is the displacement [29].

| Material properties | PA12 material |
|---|---|
| Young's modulus $E$ [GPa] | 1.47 |
| Poisson's Ratio $\mu$ [-] | 0.4 |
| Density $\rho$ [kg m$^{-3}$] | 1 010 |
| Thermal expansion $\alpha$ [K$^{-1}$] | $10^{-12}$ |
| Tension Strength $f_t$ [MPa] | 41 |
| Fracture Energy $G_f$ [kN m$^{-1}$] | 7 |

Table 5. Material properties used in the calculation [6], where the density, tensile strength and Young's modulus are values taken from the manufacturer's datasheet.

in the experiments were around 6.2–7 kN m$^{-1}$ [30, 31] for fracture energy and around 0.37–0.43 [30–33] for Poisson's ratio. The material properties used in the FEA of previous research [6] are given in Table 5.

The first simple tensile calculation was performed on the material model mentioned in Table 5. The calculation used a specimen with a width of 2.00 mm. The deformation was set as a displacement of 4 mm in the element axis and located in the middle of the extended part. The quadratic mesh with quadrilateral (hexahedra for 3D calculation) elements of size $0.25 \times 0.25$ mm in the merged part of the specimen was set for the calculation. The dimensions and shape of the numerical model were according to the specimens from the experiment.

The calculation was split into two types. The first was carried out in a 3D environment, but the outcome differed considerably from the experimental results, and the computation time for this case was extensive. Therefore, the environmental 2D calculation was performed using plane stress, where the result did not match the experiment either, but the calculation was many times faster. The differences between the computation time of the two methods are due to the number of elements, where there are fewer elements and nodes in the plane stress against the 3D problem. Figure 15 shows the calculation result compared with the experimental data.

The results showed huge differences between the FEA and the experiment data. This is due to an

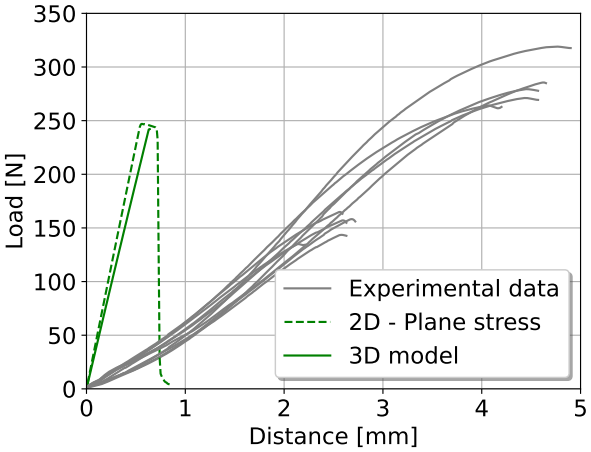


Figure 15. Comparison of experimental data and calculation results with material properties taken from the Table 5.

unsuitable chosen material model and material properties. From the first view, Figure 15 (as in Figure 2) shows that the elastic part of FEA and the experiment data did not match. The experiment showed a much lower value of Young's modulus (200–260 MPa) than the value given in the manufacturer's datasheet (1.47 GPa), which led to a parametric study of the effective Young's modulus value. In general, for 3D printing of thin samples, the values given by the manufacturer cannot be taken into account, and it is necessary to choose effective values for these samples to match reality. Therefore, a selection of the effective Young's modulus for the following FEA is needed to obtain a better agreement between the numerical analysis results and the experimental data.

The effective determination of Young's modulus $E_{\text{eff}}$ used the material model of previous calculations with a change in Young's modulus value. The appropriate chosen value should help to better fit the FEA results with experimental data and approximate the linear part behaviour to the actual behaviour from the experiments. For this reason, several models with varying values of Young's modulus (M1 – $E = 1.47$ GPa, M2 – $E = 0.47$ GPa, M3 – $E = 0.25$ GPa) were created using plane stress for faster calculations.

Figure 16 shows the load diagrams for each model with different values of Young's modulus. Model 3 with an Young's modulus value $E_{\text{eff}} = 250$ MPa best fits the experimental data, so this effective Young's modulus was used in further calculation. The effective value also corresponds to the experiment values ranging from 200 to 260 MPa, which are mentioned in Table 2. There is still a minor reservation in the result between the experimental data and FEA due to the inappropriate chosen material model (quasi-fragile material) used in the calculation.

The second thing to refining the results is the choice of a suitable material model for calculation. The calculations used for the material *Cementitious2* described a quasi-fragile material where compressive failure is

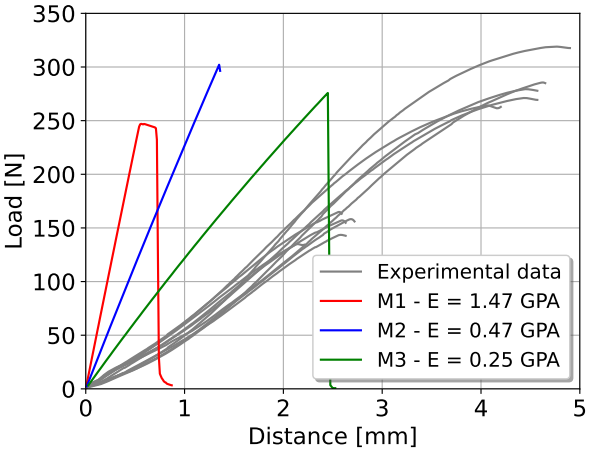


FIGURE 16. Parametric study of the value of Young's modulus with a comparison of FEA results with experimental data.

based on the theory of plasticity and the formation and propagation of cracks are based on fracture mechanics [28]. Polyamides tend to exhibit an elasto-plastic behaviour, which can be defined in material *Cementitious2-User*, where the tensile strength is characterized by a function with values corresponding to the strain.

For this reason, the material model with elasto-plastic behaviour using the *Cementitious2-User* was created. From the tensile diagram provided by the manufacturer [21] shown in Figure 17, the elastic tensile strength was determined as $f_{t,EL} = 18\,\text{MPa}$ and the elastic strain as $\epsilon_{EL} = 0.02$. The stress function can be easily solved as:

$$f_{t(\sigma_y)} = \frac{\sigma_y}{f_{u,t} - f_{y,t}} \tag{4}$$

where $\sigma_y$ is stress corresponding to the strain, $f_{u,t}$ is ultimate tensile strength determined as 41 MPa and $f_{y,t}$ is yield strength determined as 18 MPa. Then, using the dependence of the plastic strain ($\epsilon_p$) and the ratio $f_{t(\sigma_y)}$ created a plastic behaviour function where I took the values from the tensile diagram given by the manufacturer (Figure 17) and the calculated values used in FEA is shown in Figure 18.

Another calculation option is the VonMises plasticity model typically used for numerical analysis of steel structures and materials. In the calculation using this model, when the load reached a capacity, the specimens did not rupture but only stretched in the most stressed part. For the VonMises model, the tensile strength was set as $f_t = 41\,\text{MPa}$ and the hardening modulus 5 MPa. A comparison of these material models with effective Young's modulus for a 2.00 mm thick specimen is shown in Figure 19.

A material models parametric study of printed samples with elasto-plastic behaviour showed the best agreement between the experimental data and the FEA results with the *Cementitious2-User* material model, where the plastic tensile strength behaviour was described by the function. For each thickness, the calculation with this material model definition and the effective Young's modulus $E_{\text{eff}}$ was performed. Comparisons of the experimental data and FEA results for widths 0.50 mm and 2.00 mm are shown in Figure 20.

It is visible in the diagrams that the FEA results show a collapse when the load reaches maximum. This is because the tensile strength function after its peak is not described. The behaviour beyond the peak is not detailed by the manufacturer in the datasheet, and as a result, the function following the peak remains unspecified.

After determining the appropriate material model and effective Young's modulus from a simple tensile calculation, this knowledge could be used to perform a calculation that simulated the fracture toughness experiment. The numerical results of a previous research [6] dealing with a large-scale study of the fracture toughness of thin polyamide specimens showed huge differences between the numerical results and the experimental data. The tensile behaviour of the material and fracture energy $G_f$ mainly influenced the fracture toughness calculation. To improve the agreement between FEA results and experimental data, the effective Young's modulus and elasto-plastic material model were used in the calculation. This modification showed a remarkable calculation refinement, as shown in Figure 21.

The FEA fracture toughness results showed a large approximation of the results against the FEA results in previous research [6]. The result did not match perfectly, which can be noticed by the insufficient definition of others' strength functions. In the *Cementitious2-User* material model, it is possible to describe not only tensile strength as a function but also compressive, shear, and tension-compressive strengths.

## 5. Results and discussion

Previous research [6] has looked at the fracture toughness of very thin PA12 samples, where the research was divided into experimental and numerical parts. The experimental part included extensive testing of sample thicknesses ranging from 0.50 mm to 2.00 mm. Orthotropy was also included in the experiment using different printing directions. Numerical analysis was performed using the ATENA software to simulate the experiment, where the results showed huge differences between the numerical analysis and the experimental data.

The differences were most likely due to a unsuitable chosen material model and the selection of inappropriate material parameters. The quasi-fragile material model was used in the calculation, which in this case was not the correct consideration because the PA12 material has an elasto-plastic behaviour. It is well known that for thin 3D printing samples using SLS powder technology, the material properties given by

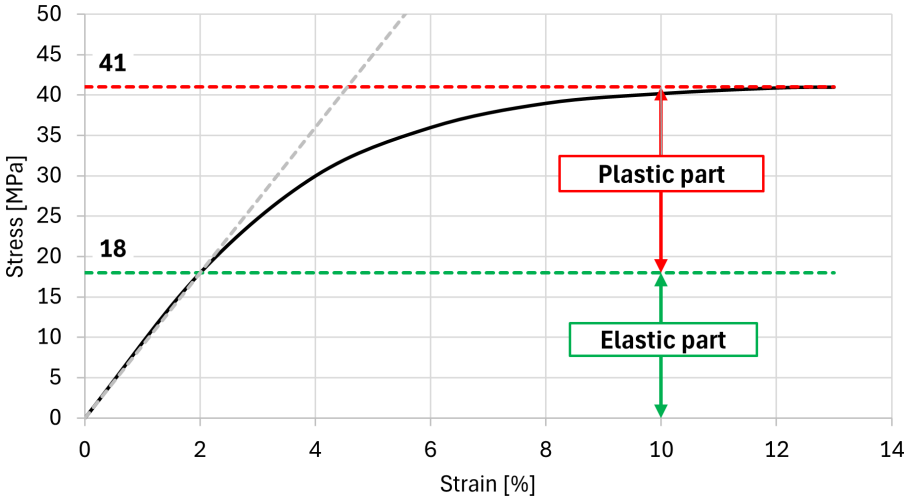


Figure 17. The stress-strain diagram of PA12 material obtained from the simple tensile experiment mentioned by Sinterir sp. z o.o. [21]. Using the tangent line in the linear part of the diagram, it was then easy to determine the elastic and plastic parts, allowing for the subsequent determination of the material's plastic behaviour within the model.

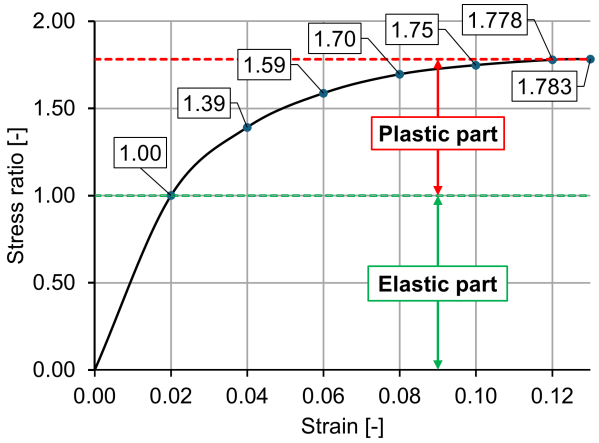


Figure 18. Diagram showing the tensile strength function used in the *Cementitious2-User* material model.

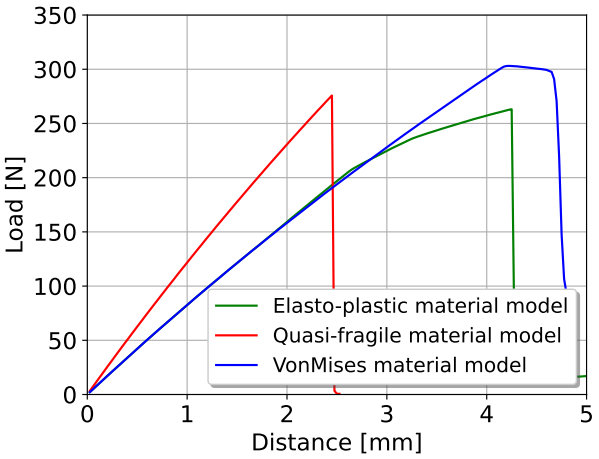


Figure 19. Parametric study of differences material models used in FEA calculation for a 2.00 mm thick specimen.

the manufacturer cannot be taken into account and effective values for these thin samples need to be determined.

The manufacturer provides insufficient information on the mechanical properties of PA12 in its datasheet. Some of the properties listed are Young's modulus and tensile strength, which can be easily determined from a simple tensile test. Therefore, this research deals with a simple tensile experiment to observe the linear part of the specimens under load, from which Young's modulus and the ultimate tensile strength for these thin specimens can be determined and then used these determined values for simple tensile and fracture toughness numerical analysis.

In both types of experiments, samples with nominal widths of 0.50 mm and 0.75 mm exhibited substantial variations and instability in the results. However, beyond a certain thickness, the measured values became more consistent and increased with thickness. For tensile and fracture toughness calculations, width is a critical parameter. Thinner specimens (0.50 and 0.75 mm) showed considerable discrepancies between the assumed and measured thicknesses. These inconsistencies can be attributed to 3D printing imperfections and ineffective welded powder balls on the surface.

In the simple tensile experiment, orthotropy was applied by varying the printing directions. However, significant defects were observed in the horizontally printed specimens, limiting the number of usable samples. In that fact, further numerical analyses were performed only for vertically printed samples.

One printing direction proved dominant for a given load type, namely that direction with layers printed parallel to the load direction. The simple tensile experiment showed increasing values due to the thickness of the specimen and significant differences between the material properties given by the manufacturer and

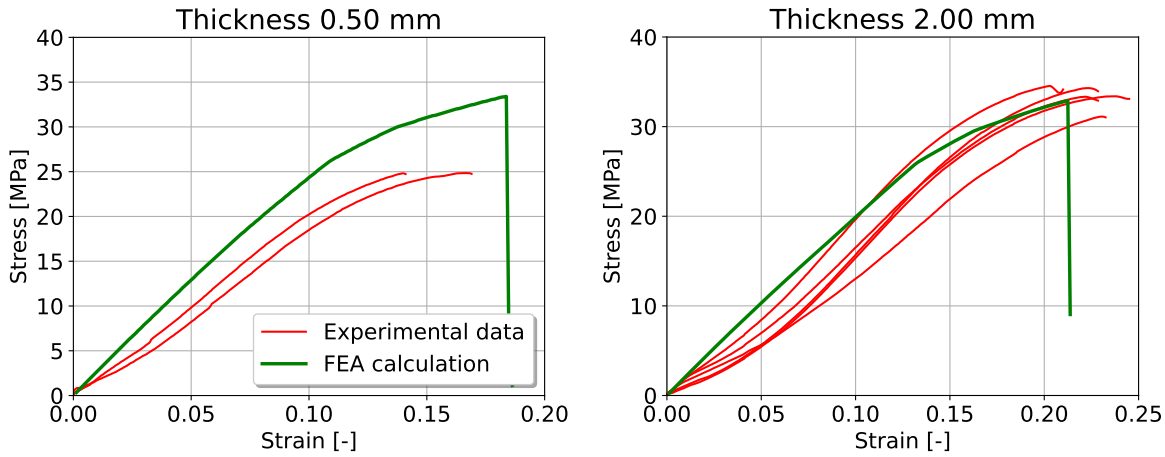


FIGURE 20. Comparison of experimental data and FEA calculation using *Cementitious2-User* material model described by a tensile strength function as the elasto-plastic material. Also the Effective Young's modulus $E_{\text{eff}} = 250\,\text{MPa}$ is used in the calculation.

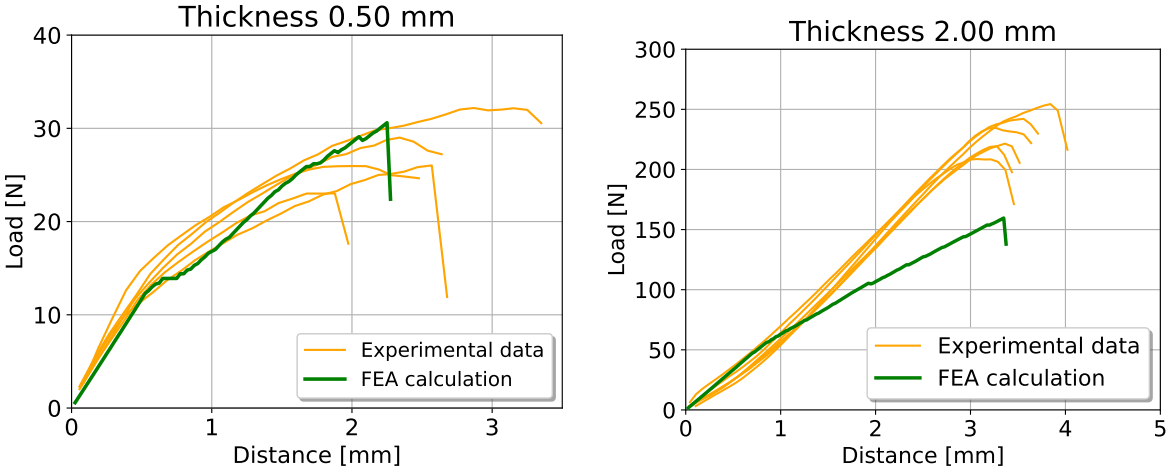


FIGURE 21. Comparison of results between FEA and experimental data in the case of fracture toughness using an elasto-plastic material model and the effective Young's modulus $E_{\text{eff}} = 250\,\text{MPa}$.

| **Material properties** | **Datasheet** | **Experiment** |
|---|---|---|
| Young's modulus $E$ [GPa] | 1.47 | 0.21–0.26 |
| Tension Strength $f_t$ [MPa] | 41 | 22–34 |

TABLE 6. Comparison of material properties given by manufacturer's datasheet versus experimental results of vertically printed samples. The increase in values in the experimental data is due to increasing sample width.

the material properties found in the experiment, as shown in Table 6. This highlights that standardized parameters may not apply to very thin samples.

After the simple tensile experiment was conducted, it was necessary to determine the effective parameters for numerical analysis. The results were validated through finite element analysis (FEA) using ATENA software [20]. Initially, a parametric study was carried out to determine the effective Young's modulus, which was found to be $E_{\text{eff}} = 250\,\text{MPa}$. This value corresponds to Young's modulus solved in the experimental data. The material model was then adjusted to be an elasto-plastic material using the *Cementitious2-User* material model. These adjustments to the material properties and material model proved to be very effective, and the results of the numerical analysis began to match the values from the experiment.

## 6. CONCLUSION

The FEA of simple tensile showed a perfect match in the values for the specimen thickness of 2.00 mm. An effective Young's modulus study was performed for this thickness, so the agreement between experimental and numerical results is favorable. For a thickness of 0.50 mm, there is already less difference in the results. Subsequently, a numerical simulation of the fracture toughness experiment was performed using the effective Young's modulus and a material model derived from the simple tensile test. The modification in the material model showed a significant improve-

ment in the correlation between the FEA results and the experimental data.

However, the FEA results still did not fully match the experimental results. This discrepancy could result from the use of a single value of the effective Young's modulus for all thicknesses. Therefore, it would be advisable for future research to establish a coefficient $\Delta_t$ that would accurately adjust the parameters for the required thicknesses. Furthermore, insufficient definition of other strength functions in the material model, which were not critical in the simple tensile test, may have contributed to the mismatch. Another limitation of the material model is its lack of a detailed description of the elasto-plastic behaviour after reaching the peak stress. All these findings on improving the numerical analysis of 3D printed polyamide samples are the main focus of further research.

## Acknowledgements

The financial support from Czech Science Foundation (project No. 23-04971S) and Czech Technical University in Prague (SGS project No. SGS23/152/OHK1/3T/11) is gratefully acknowledged.

## References

[1] A. Cheng, A. Humayun, D. J. Cohen, et al. Additively manufactured 3D porous Ti-6Al-4V constructs mimic trabecular bone structure and regulate osteoblast proliferation, differentiation and local factor production in a porosity and surface roughness dependent manner. *Biofabrication* **6**(4):045007, 2014. https://doi.org/10.1088/1758-5082/6/4/045007

[2] Q. Ran, W. Yang, Y. Hu, et al. Osteogenesis of 3D printed porous $Ti_6Al_4V$ implants with different pore sizes. *Journal of the Mechanical Behavior of Biomedical Materials* **84**:1–11, 2018. https://doi.org/10.1016/j.jmbbm.2018.04.010

[3] A. Jíra, M. Šejnoha, T. Krejčí, et al. Mechanical properties of porous structures for dental implants: Experimental study and computational homogenization. *Materials* **14**(16):4592, 2021. https://doi.org/10.3390/ma14164592

[4] L. Řehounek, A. Jíra, P. Hájková, Z. Čejka. Optimization of 3D printed trabecular structures for implantology and their mechanical analysis, 2017. Unpublished report from TAČR project No. TJ01000328.

[5] A. H. Schoen. Infinite periodic minimal surfaces without self-intersections. Tech. Rep. TN D-5541, NASA, 1970.

[6] P. Bočan. *Experimental verification of the influence of thickness on 3D printed samples on fracture toughness parameters*. Master's thesis, Czech Technical University in Prague, 2024. [2024-08-10]. http://hdl.handle.net/10467/113955

[7] A. Jíra, L. Řehounek, G. Javorská, P. Padevět. Experimental investigation of defects of thin 3D-printed plates. In *60th Annual Conference on Experimental Stress Analysis*, pp. 1–5. 2022.

[8] M. Varghese, M. W. Grinstaff. Beyond nylon 6: Polyamides via ring opening polymerization of designer lactam monomers for biomedical applications. *Chemical Society Reviews* **51**(19):8258–8275, 2022. https://doi.org/10.1039/D1CS00930C

[9] S. Shiva, R. G. Asuwin Prabu, B. Gauri, et al. A review on the recent applications of synthetic biopolymers in 3D printing for biomedical applications. *Journal of Materials Science: Materials in Medicine* **34**(12):62, 2023. https://doi.org/10.1007/s10856-023-06765-9

[10] M. Shakiba, E. Rezvani Ghomi, F. Khosravi, et al. Nylon – A material introduction and overview for biomedical applications. *Polymers for advanced technologies* **32**(9):3368–3383, 2021. https://doi.org/10.1002/pat.5372

[11] H. Kim, S. Jeong. Case study: Hybrid model for the customized wrist orthosis using 3D printing. *Journal of mechanical science and technology* **29**(12):5151–5156, 2015. https://doi.org/10.1007/s12206-015-1115-9

[12] O. A. Alo, D. Mauchline, I. O. Otunniyi. 3D-printed functional polymers and nanocomposites: Defects characterization and product quality improvement. *Advanced Engineering Materials* **24**(5):2101219, 2022. https://doi.org/10.1002/adem.202101219

[13] S. Wickramasinghe, T. Do, P. Tran. FDM-based 3D printing of polymer and associated composite: A review on mechanical properties, defects and treatments. *Polymers* **12**(7):1529, 2020. https://doi.org/10.3390/polym12071529

[14] A. G. Rodríguez, E. E. Mora, M. A. Velasco, C. A. N. Tovar. Mechanical properties of polyamide 12 manufactured by means of SLS: Influence of wall thickness and build direction. *Materials Research Express* **10**(10):105304, 2023. https://doi.org/10.1088/2053-1591/acf6f7

[15] D. Tasch, A. Mad, R. Stadlbauer, M. Schagerl. Thickness dependency of mechanical properties of laser-sintered polyamide lightweight structures. *Additive Manufacturing* **23**:25–33, 2018. https://doi.org/10.1016/j.addma.2018.06.018

[16] S.-L. Sindinger, C. Kralovec, D. Tasch, M. Schagerl. Thickness dependent anisotropy of mechanical properties and inhomogeneous porosity characteristics in laser-sintered polyamide 12 specimens. *Additive Manufacturing* **33**:101141, 2020. https://doi.org/10.1016/j.addma.2020.101141

[17] S. Aslanzadeh, H. Saghlatoon, M. M. Honari, et al. Investigation on electrical and mechanical properties of 3D printed nylon 6 for RF/microwave electronics applications. *Additive Manufacturing* **21**:69–75, 2018. https://doi.org/10.1016/j.addma.2018.02.016

[18] K. S. Randhawa, A. D. Patel. Influence of boric anhydride reinforcement on mechanical properties and abrasive wear of nylon 6. *Materials Research Express* **7**(5):055303, 2020. https://doi.org/10.1088/2053-1591/ab8ee4

[19] X. Wang, M. Jiang, Z. Zhou, et al. 3D printing of polymer matrix composites: A review and prospective. *Composites Part B: Engineering* **110**:442–458, 2017. https://doi.org/10.1016/j.compositesb.2016.11.034

[20] J. Červenka, L. Jendele, V. Červenka. ATENA program documentation. Tech. rep., Cervenka Consulting, 2014.

[21] Sinterir sp. z o.o. *PA12 Smooth – Material's Technical Data Sheet*, 2022.

[22] K. S. Randhawa, A. D. Patel. A review on tribo-mechanical properties of micro-and nanoparticulate-filled nylon composites. *Journal of Polymer Engineering* **41**(5):339–355, 2021. https://doi.org/10.1515/polyeng-2020-0302

[23] M. Shakiba, E. Rezvani Ghomi, F. Khosravi, et al. Nylon – A material introduction and overview for biomedical applications. *Polymers for advanced technologies* **32**(9):3368–3383, 2021. https://doi.org/10.1002/pat.5372

[24] L. Ladani, M. Sadeghilaridjani. Review of powder bed fusion additive manufacturing for metals. *Metals* **11**(9):1391, 2021. https://doi.org/10.3390/met11091391

[25] International Organization for Standardization. EN ISO 12737. Metallic materials – Determination of plane-strain fracture toughness, 2010.

[26] International Organization for Standardization. EN ISO 527-1. Plastics – Determination of tensile properties – Part 1: General principles, 2019.

[27] International Organization for Standardization. EN ISO 527-2. Plastics – Determination of tensile properties – Part 2: Test conditions for moulding and extrusion plastics, 2012.

[28] S. Akram, Q. U. Ann. Newton Raphson method. *International Journal of Scientific & Engineering Research* **6**(7):1748–1752, 2015.

[29] S. Antoniou, R. Pinho. *Engineering Dynamics and Vibrations*, chap. Nonlinear Seismic Analysis of Framed Structures: Recent Developments, pp. 268–301. CRC Press, 2018. https://doi.org/10.1201/9781315119908-8

[30] A. Salazar, A. J. Cano, J. Rodríguez. Mechanical and fatigue behaviour of polyamide 12 processed via injection moulding and selective laser sintering. Analysis based on Kitagawa-Takahashi diagrams. *Engineering Fracture Mechanics* **275**:108825, 2022. https://doi.org/10.1016/j.engfracmech.2022.108825

[31] A. J. Cano, A. Salazar, J. Rodríguez. Effect of temperature on the fracture behavior of polyamide 12 and glass-filled polyamide 12 processed by selective laser sintering. *Engineering Fracture Mechanics* **203**:66–80, 2018. https://doi.org/10.1016/j.engfracmech.2018.07.035

[32] N. Lammens, M. Kersemans, I. De Baere, W. Van Paepegem. On the visco-elasto-plastic response of additively manufactured polyamide-12 (PA-12) through selective laser sintering. *Polymer Testing* **57**:149–155, 2017. https://doi.org/10.1016/j.polymertesting.2016.11.032

[33] L. Cobian, M. Rueda-Ruiz, J. P. Fernandez-Blazquez, et al. Micromechanical characterization of the material response in a PA12-SLS fabricated lattice structure and its correlation with bulk behavior. *Polymer Testing* **110**:107556, 2022. https://doi.org/10.1016/j.polymertesting.2022.107556